Attosecond metrology: from electron capture to future signal processing

Ferenc Krausz[1,2] and Mark I. Stockman[1,2,3]

The accurate measurement of time lies at the heart of experimental science, and is relevant to everyday life. Extending chronoscopy to ever shorter timescales has been the key to gaining real-time insights into microscopic phenomena, ranging from vital biological processes to the dynamics underlying high technologies. The generation of isolated attosecond pulses in 2001 allowed the fastest of all motions outside the nucleus — electron dynamics in atomic systems — to be captured. Attosecond metrology has provided access to several hitherto immeasurably fast electron phenomena in atoms, molecules and solids. The fundamental importance of electron processes for the physical and life sciences, technology and medicine has rendered the young field of attosecond science one of the most dynamically expanding research fields of the new millennium. Here, we review the basic concepts underlying attosecond measurement and control techniques. Among their many potential applications, we focus on the exploration of the fundamental speed limit of electronic signal processing. This endeavour relies on ultimate-speed electron metrology, as provided by attosecond technology.

Attosecond science represents the culmination of the long-standing investigation of fast-evolving phenomena in nature. After the concepts of pump–probe spectroscopy[1] and optical synchronization[2] were introduced in the nineteenth century, subsequent progress in improving the temporal resolution of time-resolved measurements was dictated by the development of light sources capable of producing ever-shorter pulses and of techniques for their measurement. Several technological revolutions were required to advance ultrafast science from the nanosecond scale, which can be accessed by incoherent light sources, to the femtosecond regime, and eventually to the attosecond regime. The laser[3,4] (for which Basov, Prokhorov and Townes were awarded the Nobel Prize in Physics in 1964) provided the basis for all these advances, thanks to its ability to emit perfectly sinusoidal light waves over many seconds, which consist of quadrillions (10^{15}) of identical wave cycles. This coherence opened the door for measuring time over long periods and brief intervals with unprecedented precision and resolution, respectively.

Perturbative nonlinear optical effects[5,6] (for which Bloembergen was awarded the Nobel Prize in Physics in 1981) allow the optical properties of materials, such as their refractive index and absorptivity, to be varied as a function of the cycle-averaged intensity of intense laser radiation. Some of these changes can be harnessed to create light modulators, which alter the phase and/or amplitude of transmitted or reflected laser light in proportion to its intensity. Integrating such a device in a broadband laser oscillator permits the eigenmodes of the laser cavity modes to be phase locked. A second revolution, namely in nonlinear optics[7], thus led to the generation of femtosecond laser pulses[8]. By the turn of the millennium and some 15 years after the seminal report on three-cycle optical pulses by Shank and co-workers[9], the evolution of femtosecond technology approached its ultimate limit — the wave cycle[10]; this was achieved through realizing broadband dispersion control using chirped multilayer mirrors[11] (Fig. 1). The envelope of the fastest, few-femtosecond laser pulses is short enough to temporally resolve any molecular dynamics[12] (for which Zewail was awarded the Nobel Prize in Chemistry in 1999), but it is insufficient to capture atomic-scale electronic motion.

Strong-field interactions driven by few-cycle light pulses[10] enabled the electronic responses of matter to be controlled and
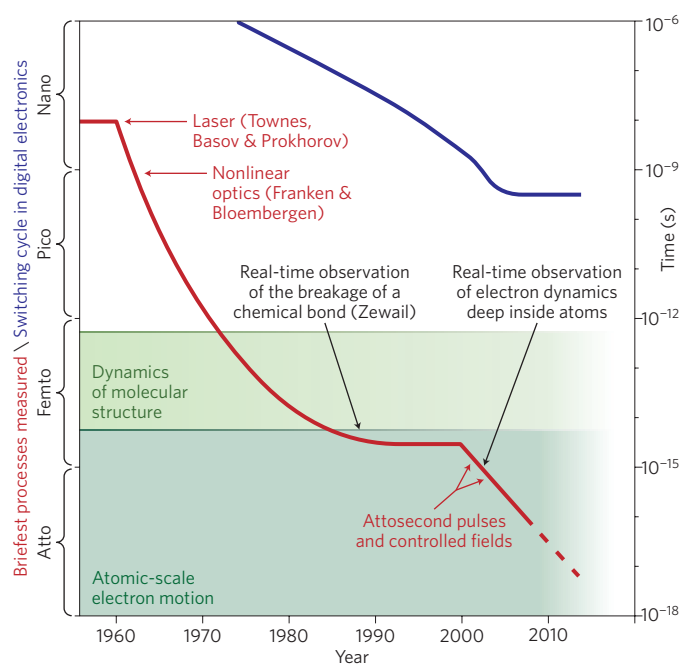

Figure 1 | Evolution of ultrafast science and digital electronics. Briefest measured time intervals (lower red line) and shortest switching cycle (inverse of the clock rate) of digital processors (upper blue line). Discontinuities in the derivative of the briefest measured interval against year curve indicate revolutions in ultrafast metrology. In the early 1960s, coherent light waves generated by lasers and nonlinear optical effects were used to produce ultrashort pulses from these waves. At the beginning of the new millennium, attosecond pulse generation and measurement[18] were realized, and controlled light fields for precision attosecond control[28] and metrology[34] were generated.

measured within an optical cycle, that is, on an attosecond timescale. Just as cycle-averaged-intensity-driven perturbative nonlinear optics had led to femtosecond pulses, nonperturbative

[1]Fakultät für Physik, Ludwig-Maximilians-Universität, Am Coulombwall 1, D-85748 Garching, Germany, [2]Max-Planck-Institut für Quantenoptik, Hans-Kopfermann-Strasse 1, D-85748 Garching, Germany, [3]Department of Physics and Astronomy, Georgia State University, Atlanta, Georgia 30303, USA.
e-mail: krausz@lmu.de; mstockman@gsu.edu

nonlinear optical effects governed by a strong, oscillating field, such as above-threshold ionization[13] and high-order harmonic generation (HHG)[14–17] spawned extreme ultraviolet (XUV) light pulses lasting less than 1 fs (ref. 18); this represents the latest revolution in ultrafast science[19,20] (Fig. 1).

The field–matter interactions underlying attosecond technology are sensitive to the subcycle evolution of the optical field, $F_L(t) = F_0\, a(t)\, \exp[-i(\omega_L t + \varphi_{CE})] + c.c.$, where F_0 is the peak electric field, $a(t)$ is the normalized amplitude envelope, ω_L is the carrier frequency, φ_{CE} is the carrier-envelope phase (CEP) and c.c. is the complex conjugate. Some four decades after the invention of the laser, the field oscillations 'underneath' the amplitude envelope became relevant[21]. The timing of field oscillations with respect to the pulse peak set by the CEP fluctuates in a femtosecond laser[22] simply because the (perturbative) nonlinear optical effects responsible for laser mode locking are insensitive to the CEP. Broadening of the mode-locked laser spectrum to a full octave and self-interference of the radiation with its second harmonic[23] provided access to the quasi-periodic evolution of the CEP[24] in the emitted femtosecond pulse train and allowed it to be locked to a radiofrequency reference[25,26]. The resultant phase-coherent link between the radiofrequency signals and the optical radiation allowed this locked optical frequency comb to connect atomic transitions, which have the potential to be used as optical frequency standards, with radiofrequency electronic signals driving clocks[27] (Hänsch and Hall were awarded the Nobel Prize in Physics for this work in 2005). The radiofrequency control of the mode-locked frequency comb and subsequent amplification and pulse compression provided intense, CEP-stabilized (that is, waveform-controlled), few-cycle light pulses[28].

Attosecond pulse generation and measurement

The electric field of an intense waveform-controlled, few-cycle light pulse[28] exerts a force on electrons that rivals intra-atomic (Coulomb) forces and can be varied in a controlled fashion on the electronic timescale. This attosecond force can be shaped within the wave cycle to an extent that depends on the relative bandwidth, $\Delta\omega/\omega_L$, of the light pulse. For a sub-octave bandwidth ($\Delta\omega/\omega_L < 1$), adjustment of the CEP provides a means of shaping the field evolution within the field cycle. Although it is quite weak even for a two-cycle pulse (Fig. 2a), this shaping is crucial for reproducible generation of isolated attosecond pulses by HHG[29] (Fig. 2b,c). Control of the field evolution within the wave cycle permits attosecond control of the three steps involved in the emission of attosecond XUV pulses — tunnel ionization, excursion of the quasi-free electron and its recollision with the parent ion[30–33]. It thus enables the parameters of attosecond laser pulses to be precisely reproduced from one pulse to the next.

Waveform control is equally important for temporal characterization. In fact, it is the controlled, attosecond variation of the laser electric field that maps the temporal profile of the attosecond pulse to a final momentum distribution of photoelectrons[34] in the light-field-driven (or attosecond) streak camera[35,36] (Fig. 3). Recording photoelectron spectra for varying timings of the attosecond pulse with respect to the streaking field provides complete information about the temporal intensity profile and chirp of the attosecond pulse as well as the electric field in a few-cycle wave[37–40].

Trains of attosecond pulses and their first applications

Electron dynamics confined to less than one laser period can also be time resolved by attosecond pulse trains, which were first generated in 2001[41–43]. Alternatively, the harmonic emission produced by the recolliding electron may also serve as a probe[44]. In these measurements, the dynamics is re-triggered each cycle by the next attosecond burst or by the next period of the strong laser
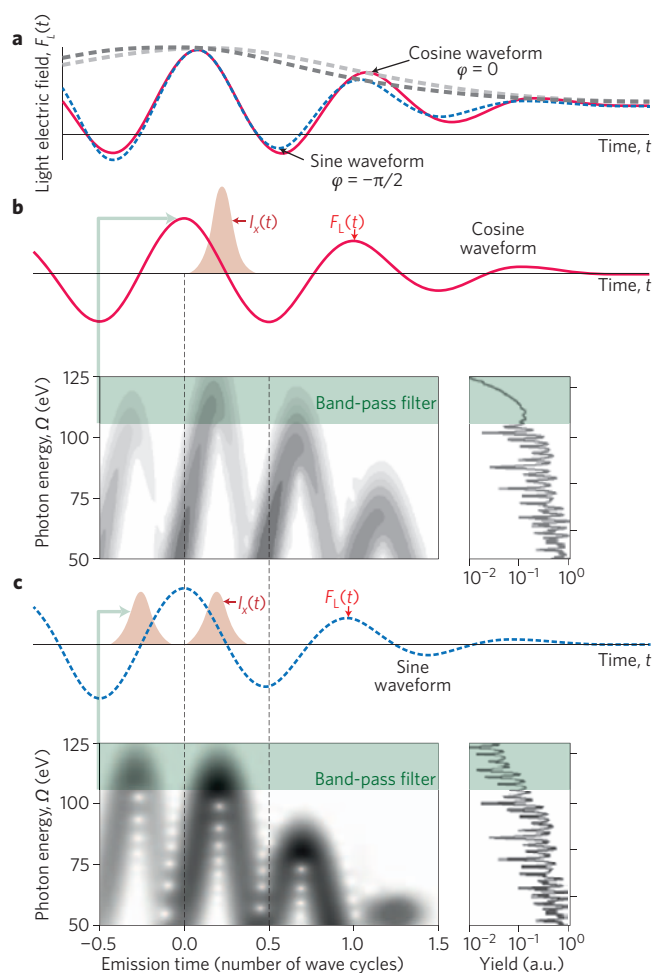

Figure 2 | Prediction of attosecond XUV pulses. a–c, Computations by V. Yakovlev predicted the emission of attosecond XUV pulses from neon atoms irradiated by NIR laser fields (wavelength, 750 nm). These pulses contain two oscillation cycles within the 5-fs full-width at half-maximum of their intensity envelope (**a**) for a cosine (red solid lines in **a** and **b**) and sine (blue dashed lines in **a** and **c**) waveforms; despite the fact that these two waveforms differ only slightly, they are predicted to lead to an isolated XUV pulse and a twin attosecond XUV pulse, respectively. Figure courtesy of V. Yakovlev. Figure adapted with permission from ref. 125 © 2007 NPG.

field. Consequently, the physical observables are accumulated over many sub-laser-cycle pump–probe exposures, and hence variations in physical parameters (such as the laser field amplitude and the probe pulse duration) over this multicycle signal accumulation should be minimized. In a series of carefully performed experiments[45–50], the attosecond dynamics of electron wave packets launched by an attosecond pulse train in atoms and molecules were traced by the multicycle field previously used to generate the attosecond pulse train. Subcycle processes periodically triggered by multicycle fields in atoms and molecules can be efficiently interrogated by the sub-femtosecond recolliding electron wave packets extracted from the sample under scrutiny by strong-field ionization. In this powerful approach, the multicycle wave both generates the recolliding electron probe and triggers the subcycle process under study in a correlated fashion, leaving no room for any timing jitter between the pump and the probe. The generated high-order harmonics and photoelectrons provide unprecedented insight into the attosecond electron dynamics and accompanying molecular dynamics[51–65].

Tracing electrons with isolated attosecond pulses

Waveform-controlled, few-cycle laser pulses[28] and the reproducible isolated attosecond pulses they spawn[34,66,67] constitute an enabling technology for both precision attosecond metrology of light signals and real-time access to a vast variety of electron processes that unfold on the attosecond timescale and extend over the femtosecond timescale. Figure 4 displays these tools at the heart of a state-of-the-art attosecond system. Sub-4-fs, near-infrared (NIR), 750-nm-carrier-wavelength laser pulses produce sub-100-attosecond XUV pulses in the 100-eV photon energy range via HHG in neon gas. An attosecond electron streak camera records the streaking spectrogram (shown in the inset in Fig. 4), which allows both the sub-4-fs laser waveform and the 72 as XUV pulse (depicted on the optical axis) to be retrieved. Arriving in perfect synchrony with each other, they (or their slightly longer predecessors) allow a variety of pump–probe techniques to be performed, including attosecond streaking[68,69] and tunnelling spectroscopy[70] in which the XUV pulse is used as the trigger and the controlled laser field as the probe. They also provide real-time insight into multi-electron relaxation processes in highly excited atoms, such as a cascaded Auger decay[70] and intra-atomic electron correlations implying a delay in photoemission[69].

In a similar scheme, attosecond photoelectron spectroscopy provides access to details of atomic ionization[71,72] as well as structural and electronic wave-packet dynamics in simple molecules[73,74]. Alternatively, strong-field processes induced by a controlled laser waveform can be tracked by attosecond transient absorption spectroscopy by using the XUV pulse as the probe[75]. Attosecond transient absorption measurements on krypton atoms ionized by a near-single-cycle NIR field have revealed for the first time electron tunnelling within a fraction of a half wave cycle, an instantaneous optical-field-induced Stark shift of valence levels, and the emergence of coherent valence electron wave packet dynamics in an ion ensemble[76]. These experiments provide compelling evidence that the basic attosecond tools and techniques work well and that they have become mature enough for their application to extend to condensed matter.

Attosecond physics of condensed matter

Attosecond processes in solids were first accessed experimentally by using a short-lived core hole in an adsorbed sulphur atom as a clock[77]. The first attosecond time-resolved study[68] was performed on monocrystalline tungsten using attosecond streaking[35]. It revealed that electrons originating from localized core states of tungsten arrived at the tungsten surface with a ~100 as delay relative to those freed from delocalized conduction-band states. In contrast, for monocrystalline magnesium, photoelectrons originating from the core and valence-band states arrived simultaneously at the surface, within the experimental uncertainty of 20 as (ref. 78). Comparison of these experimental results with theoretical investigations[79–86] suggests that the observed delays originate from electron propagation. If so, the new method may be dubbed attosecond electron-propagation chronoscopy; it appears to be a sensitive probe of the high-energy band structure and a promising approach for exploring atomic-scale electron transport phenomena near surfaces.

Internal strong-field photoionization (breakdown) of insulators[87] is expected to follow the instantaneous excitation field and hence be CEP dependent, as predicted earlier for photoemission from metal nanostructures[88]. The first experimental observation of strong-field photoemission from tungsten nanotips[89] confirmed this prediction, as did a more recent study of gold nanotips[90]. A subsequent investigation[91] of strong-field emission from a plasmonic (gold) nanotip at local field strengths of approximately < 2 V Å^{-1} established a new effect — a very short localization
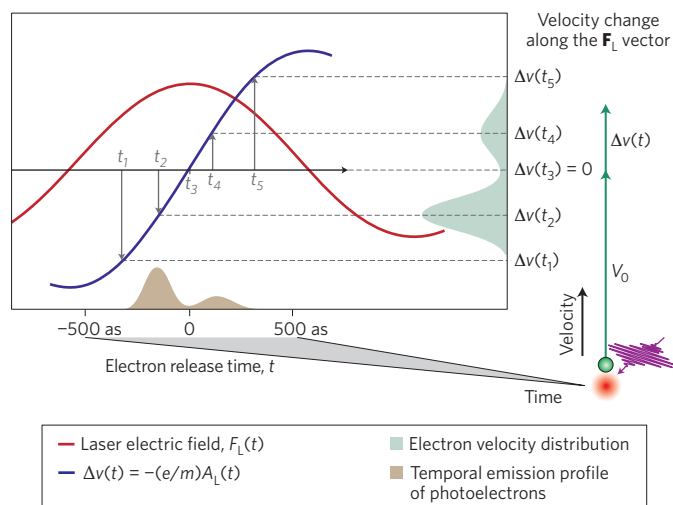

Figure 3 | **Concept of light-field-driven attosecond streaking.** Photoelectrons released by an attosecond XUV pulse in the presence of a strong linearly polarized laser field (red line) parallel to the electric field vector suffer a change in their velocity that is proportional to the vector potential of the field (blue line) at the moment of release. Here, $\Delta v(t)$ is proportional to the vector potential of the electric field, $A_L(t)$. This change in the final velocity is monotonic within a half wave cycle of the field, and maps the intensity profile of the sub-femtosecond XUV pulse to a corresponding final velocity distribution of photoelectrons. Recording these 'streaked' photoelectron spectra as a function of time delay with respect to the streaking field yields a streaking spectrogram (see Fig. 4), from which the attosecond XUV pulse profile and chirp as well as the laser waveform can be retrieved. Figure adapted with permission from ref. 20; © 2009 APS.

radius of the nanoplasmonic field at the tip permits an electron to escape from the nanolocalized region within a fraction of an optical cycle (that is, on a timescale of hundreds of attoseconds), effectively suppressing ponderomotive oscillations. As Stockman et al.[92] proposed, this allows a photoelectron ejected by an attosecond XUV pulse to probe directly the local electric field; this is in contrast with gas-phase attosecond streaking experiments[34], which probe the vector potential of the local electric field (that is, its time integral). Attosecond probing of nanoscopic electric fields will provide direct access to ultrafast nanoplasmonics in space and time.

These novel attosecond techniques may be instrumental in investigating ways to overcome the speed limits of contemporary digital electronics and explore the ultimate limits of electron-based signal processing.

Frontiers of electronic signal processing

The basic building blocks of contemporary digital electronics are metal–oxide–semiconductor field-effect transistors (MOSFETs)[93]. Although high-speed MOSFETs function up to cutoff frequencies f_{cutoff} in the approximate range 100 GHz–1 THz (refs 94–103), the maximum speed (the clock rate in engineering terminology) of processors has been limited to $f_{processor} \approx 3$ GHz for more than a decade (see Fig. 1). This limitation is a result of the charging time, $\tau_{charging} \lesssim 100$ ps of the interconnect wires that couple the transistors to form a processor; specifically, $f_{processor} \approx \tau_{charging}^{-1}$ (Fig. 5; for more details, see Box 1). Yet another limitation originates from heat dissipation, which mainly occurs in contemporary digital electronics when a transistor recharges the interconnect wire. The energy dissipated during this process per switching cycle for a long (~5 mm) interconnect is of the order of $Q_{switch} \approx (1/2)$
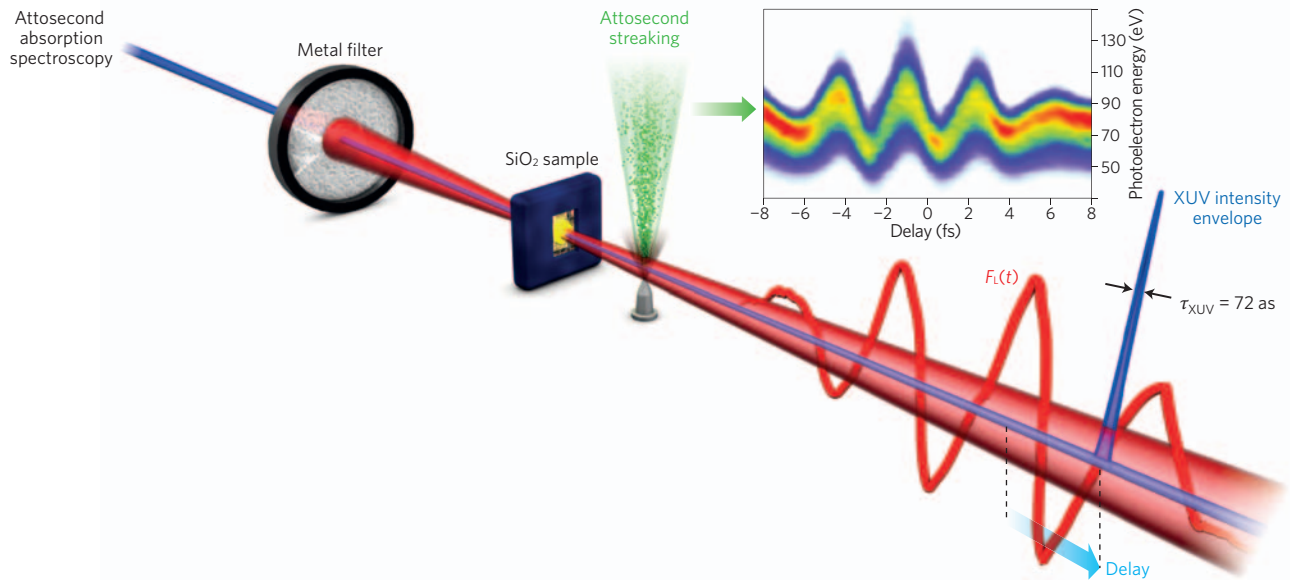
Figure 4 | Tools of attosecond metrology and spectroscopy. Sub-4-fs, sub-1.5-cycle NIR laser pulses and synchronized near-70-as XUV pulses retrieved from the attosecond streaking spectrogram (shown in the inset). Simultaneous streaking and attosecond probe (here, absorption) spectroscopy permit attosecond timing of the attosecond snapshots (here, transient absorption spectra) to the strong excitation field triggering electron motion (as shown in Fig. 6). Figure adapted with permission from ref. 110 © 2013 NPG.

$C_{interconnect}(\Delta U_{gate})^2 \approx 1$ fJ. The processor clock rate is determined by long interconnects, whereas the average energy per switch per transistor is determined by a typical (~500 μm) interconnect, and is an order of magnitude smaller ($Q_{switch} \approx 0.1$ fJ). This gives an upper limit for the power consumption per processor $P_{processor} \approx N_t f_{processor} Q_{switch} \approx 300$ W, where $N_t \approx 10^9$ is the number of transistors in the processor. This upper limit is several times higher than typical power consumptions ($P_{processor} \approx 100$ W), because not all transistors switch all the time. Such a high power consumption presents problems both for heat management and the combined energy cost of existing computers that already significantly load the power grid, constituting another severe challenge for scaling current digital electronics to much higher clock rates and transistor numbers.

Optical on-chip interconnects are promising for circumventing these limitations[104]. As these interconnects need to be the same size as the transistors themselves, deeply subwavelength structures that rely on plasmonic nanoconfinement are required[105–107]. The bandwidth of nanoplasmonic structures extends over the entire visible spectrum into the mid-infrared range[105], resulting in a response time of $\tau_{response} \lesssim 1$ fs. Hence, future plasmonic interconnects may, in principle, open the door for scaling the signal processing (clock) frequency towards the petahertz frontier, and research and development of these systems may benefit from the attosecond techniques described in the previous section. However, the speed of MOSFETs, which is limited by the mobility, recombination time and plasma frequency of the carriers[95–99,102,103], is unlikely to substantially exceed ~1 THz. Hence, novel concepts are required to approach the petahertz frontier.

The response time of a physical system is determined by its bandwidth according to $\tau_{min} \lesssim \Delta\omega^{-1}$. To use this bandwidth without major losses, the signal should spectrally be confined within the bandgap, which imposes another condition, $\Delta\omega \lesssim \Delta_g$; this implies that $\tau_{min} \lesssim \Delta\omega^{-1}, \Delta_g^{-1}$. Dielectrics such as silica and alumina and wide-bandgap semiconductors such as GaN and diamond with bandgaps in the approximate range of 5–10 eV possess the fastest responses, potentially of the order of several hundred attoseconds.

However, they require strong fields to induce changes in their electronic and optical properties. The recent demonstration of HHG induced by a strong ($F_0 = 0.2$–0.6 V Å^{-1}) mid-infrared field in a crystal of the wide-bandgap semiconductor ZnO (ref. 108) up to frequencies in the VUV range has revealed nonlinear photocurrents in the solid with an oscillation time on a ~100 as timescale.

Indirect experimental evidence of attosecond photogeneration of carriers in silica was provided by an observed change in the ellipticity of a laser pulse[109]. These experiments also suggest that for sufficiently short pulses ($\lesssim 40$ fs), the electron dynamics is not distorted by collisions.

The attosecond response of wide-bandgap materials has recently been confirmed in an attosecond time-resolved experiment seeking to track changes in the band structure and/or population dynamics induced in silica by a strong, few-cycle NIR field[110]. An attosecond XUV probe pulse traversing the sample promoted electrons from the L-shell of silicon to the conduction band of silica. Figure 6 shows a line out of the recorded transient

Box 1 | Clock rate in contemporary semiconductor electronics

The interconnect-limited processor speed (clock rate) is given by $f_{processor} = \tau_{charging}^{-1} = I_{drive}/(C_{interconnect}\Delta U_{gate})$, where $C_{interconnect}$ is the interconnect capacitance, ΔU_{gate} is the gate potential difference and I_{drive} is the drive current produced by the transistor. Modelling the interconnect as a cylinder of radius a and length L in a medium of permittivity U, results in $C_{interconnect} \approx \varepsilon L/[2\ln(L/a)]$, where $L >> a$ (ref. 122). Using realistic parameters[123], $I_{drive} = 30$ μA and $\Delta U_{gate} = 0.3$ V, and assuming $L \approx 1$ mm, $\varepsilon \approx 6$ and $a \approx 30$ nm, we obtain $f_{processor} \approx 3$ GHz. This is very close to the actual processor speed limit and is two orders of magnitude slower than the transistor speed. Dissipation of electrostatic energy during recharging of the interconnects was found to reduce the energy efficiency of the processor by three orders of magnitude with respect to that of the transistors[124].
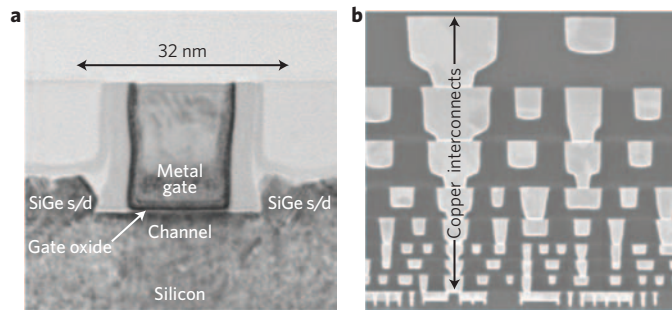
**Figure 5 | Electron micrographs of Intel processor chip and MOSFETs in it.
a**, Transistor cross-section, where "s/d" indicates the source and drain.
b, Copper interconnect wires (one of which is labelled) are visible in the
processor cross-section (vertical size is a few millimetres). The MOSFETs
are at the very bottom of this micrograph. Figure adapted from ref. 126
© 2011 Intel.

absorption spectrum at the band edge; it exhibits an instantaneous, highly reversible, transient decrease in the XUV absorptivity that oscillates in synchrony with the strong field. This suggests that this dynamics follows the instantaneous electric field, and is dominated by instantaneous changes in the local density of the conduction-band states and its virtual population rather than real transfer of population, which would survive for picoseconds (see also the caption of Fig. 6c). Note that the total conduction-band population (the sum of the virtual and real populations) is given by equation (10) in the supplementary information of ref. 110 (see also the next section). The dominance of the virtual conduction band population over the real conduction band population is also corroborated by the theoretical prediction shown in Fig. 6c. The real population can be identified as the conduction-band population that survives for delays exceeding the pulse duration. This residual value happens to be much smaller than the peak value of the total transient population, which is thus predicted to be dominated by virtual population. This conclusion appears to contradict that drawn from the recent analysis of second-harmonic emission from dielectrics[111]. It has far-reaching implications for potential signal processing and metrology applications.

Controlling the electric and optical properties of dielectrics at optical frequencies

Unlike in metals, electric fields can penetrate and charge gradients can build up in semiconductors as a result of their moderate band-gaps ($\Delta_g \lesssim 1$ eV). This forms the basis of contemporary digital electronics[93–96,112]. The above-mentioned recent attosecond study on silica[110] revealed that strong optical fields can substantially modify the electronic structure of wide-bandgap materials on a near-1-fs timescale, making them promising for developing a fundamentally new approach to electric and photonic signal manipulation, which may be largely free from the limitations of contemporary valency MOSFETs discussed above.

For fields with strengths approaching the critical field strength, $F_{crit} = \Delta_g/ea$ (where a is the lattice constant and e is the electronic charge) varying adiabatically to fulfil the condition $\omega_L << \Delta_g/\hbar$ (where $\hbar$ is the reduced Planck constant) electronic states of the solid are predicted to undergo Wannier–Stark (WS) localization[113] within approximately one unit cell of the crystal. For dielectrics such as silica and alumina with $\Delta_g \approx 9$ eV, F_{crit} will be approximately 2 V Å^{-1}, and the condition $\omega_L << \Delta_g/\hbar$ will be satisfied up to near-infrared and visible frequencies. WS localization and formation of the WS energy ladder then occurs. The energy of a WS state residing at a certain site $l = 1, 2, ...$ (where l is the site number
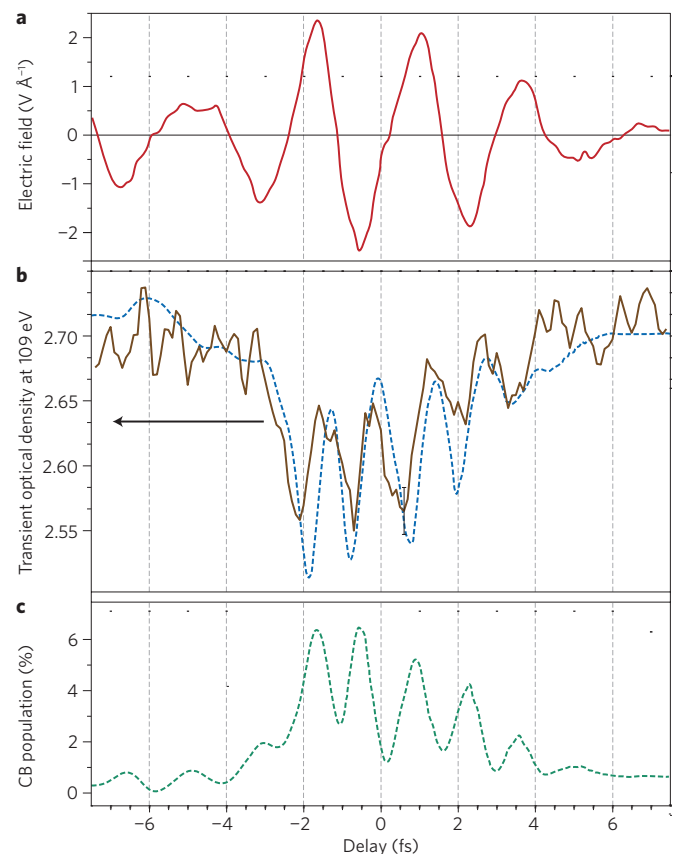

**Figure 6 | Attosecond time-resolved, strong-field-induced effects in
SiO$_2$. a**, Electric field of a few-cycle NIR laser pulse impinging on a SiO$_2$
sample, $F_L(t)$, as extracted from attosecond streaking (see Fig. 4). **b**,
Transient change in the optical density integrated over a 1-eV bandwidth
at $\hbar\omega = 109$ eV probed by the 72 as XUV pulse shown in Fig. 4 and
timed to the NIR excitation field shown in **a** by simultaneous attosecond
streaking. This allows the measured transient observable (in this case, the
absorptivity) to be assigned to well-defined moments in the excitation
field. Simultaneous attosecond probe spectroscopy and streaking thus
provide unprecedented insight into strong-field electron processes.
c, Computed transient evolution of the instantaneous population of
(unperturbed) conduction-band (CB) states timed to the laser field. The
dominant part of the conduction-band population, which oscillates as a
function of the delay, is termed the virtual population in ref. 114 (it was
originally introduced in refs 115–118). Figure adapted with permission from
ref. 110 © 2013 NPG.

expressed in terms of the lattice period) of the lattice along the direction of the internal field F becomes $E_{l,n} = E_n - eaFl$, following the field variation adiabatically. (Here, E_n with $n = \{c, j\}, \{v, k\}$ is the offset of the jth and kth subbands of the conduction and valence bands, respectively; for simplicity, we suppress the subband indices j and k in the present discussion.) The adjacent levels in each WS ladder are separated by the Bloch frequency, $\omega_B = |eF|a/\hbar$. For $F \rightarrow F_{crit}$, by definition, $\hbar\omega_B \approx \Delta_g$, and hence the Bloch frequency will be in the ultraviolet range. At this point, according to $E_{l,n} = E_n - eaFl$, $E_{l,c}(F)$ and $E_{l,v}(F)$ will become nominally equal for $\Delta l = |l_c - l_v| = 1$; that is, the WS states residing at neighbouring sites in the conduction and valence bands will become degenerate in energy to undergo an anticrossing. The calculated level diagram for silica[114] (see Fig. 7) reveals a large energy gap ΔE_1 at $\Delta l = 1$. The corresponding anticrossing gap is much larger than the NIR laser photon energy. This implies that the WS state belonging to the

lower anticrossing level remains fully occupied while adiabatically changing its wavefunction from the valence band to the conduction band (this is the well-known adiabatic exchange of quantum numbers). Consequently, the dynamics is largely reversible.

This gradual change can be quantified by projecting the actual filled, time-dependent valence-band states to zero-field conduction-band states (see equation (10) in the supplementary information of ref. 110). This projection results in the transient population of conduction-band electrons shown in Fig. 6c, and the corresponding valence-band holes. These electrons and holes can be interpreted as virtual carriers, similar to those responsible for virtual photoconductivity in semiconductors, which was theoretically predicted[115–117] and experimentally observed[118] over two decades ago. However, the analogy stops there. In the present case, the virtual carriers are produced by a nonresonant (adiabatic), strong-field (and thus, necessarily, nonperturbative) excitation; this contrasts with the early experiments in which the virtual carriers were excited by a near-resonant perturbative excitation. The virtual carriers make the system more polarizable in a static electric field[115–117] and also at optical frequencies. If so, they can help qualitatively understand both the transient reflectivity shown in Fig. 3b of ref. 110 and the transient current presented in Fig. 3 of ref. 119. Note that our conclusion on the reversibility of the photoinduced changes in dielectrics is generally incompatible with perturbation theory. In particular, the reversibility is at odds with the analysis in ref. 120, because processes proceed in one direction only in any perturbation theory. Specifically, the population is transferred from the almost completely filled valence band to the weakly populated conduction band, and the photoinduced changes are not reversible — the probability of reverse transfer from the conduction band to the valence band decreases in proportion with the conduction-band population. Thus, in perturbation theory, the excited-state population should continuously increase with every half cycle of the field, in disagreement with both the experimental results and the theory presented in ref. 110.

In the originally introduced picture[110,119], the strong but deeply adiabatic optical fields create a new state of matter in which the states of the original valence and conduction bands are mixed and the spectrum shows the formation of WS ladders and their anticrossings. In addition, population transfer between the valence and conduction bands occurs reversibly (see Fig. 7). The most significant adiabatic population transfer occurs at $\Delta l = 1$. Consequently, the original bandgap of the dielectric disappears as the energies of the occupied and empty states overlap. Thus, the pronounced Fermi surface separating the filled and empty states disappears. Because of this bandgap collapse, such a non-equilibrium state has a high polarizability; in particular, the optical conductivity is over 18 orders of magnitude higher than that of the original dielectric, reaching levels typical of semimetals[119] (it is still several orders of magnitude lower than the conductivity of a good metal). Such a non-perturbative phenomenon can
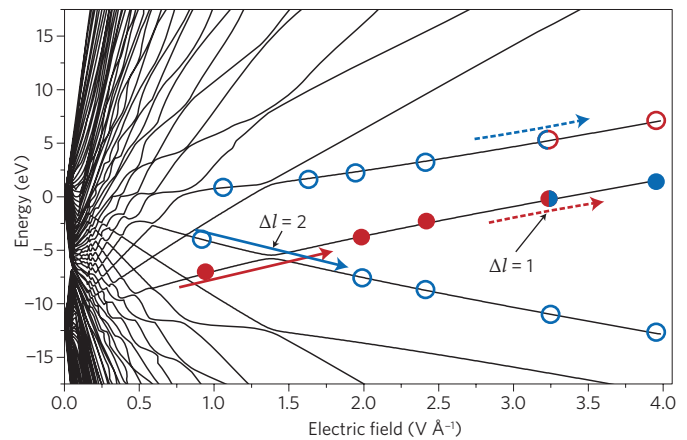

Figure 7 | Adiabatic energy spectra of valence and conduction bands for silica in strong fields. These are shown for a crystal with 50 unit cell thickness as a function of the electric field for an interband dipole moment $Z_{v1,c1}$ of 3 eÅ. The anticrossings with $\Delta l = 1$ and $\Delta l = 2$ are indicated. Red and blue circles denote levels with valence and conduction band wavefunctions, respectively. Closed and open circles represent filled and empty states, respectively. The solid crossed and dashed parallel arrows indicate level anticrossings passed diabatically and adiabatically, respectively. Figure adapted with permission from ref. 114 © 2014 NPG.

thus be termed semi-metallization. Note that the last anticrossing at $\Delta l = 1$ is only approached but not passed at the fields applied, as the field required for the full passage ($F_0 \lesssim 3.5$ V Å^{-1}) exceeds the current breakdown threshold. If the $\Delta l = 1$ anticrossing were passed without breakdown, the dielectric would have undergone a full metallization transition.

Towards petahertz-scale solid-state technology

The nonlinear polarization induced by the instantaneous optical field can be used to modulate optical signals and electric currents via strong-field-induced changes in the reflectivity (or phase delay)[110] and strong-field-induced charge separation[119], respectively. The underlying physical mechanisms differ fundamentally from those responsible for signal processing in MOSFETs where real carriers transport electric current and dissipate heat. In contrast, the strong-field effects described above create predominantly virtual carriers and offer the potential to manipulate signals in a largely reversible fashion. Dissipation originates from only the residual (real) carriers left behind by the strong few-cycle field. Maximizing the ratio of the peak to residual density of carriers, n_{peak}/n_{res} (~7 in Fig. 6c), would obviously minimize the dissipation per switching cycle and might provide a route to greatly increase the processing speed. An additional avenue to increase the energy efficiency of processing, albeit at the expense of a lower ultimate speed, is reducing the laser

---

Box 2 | Heat dissipation and power requirements of prospective 'dielectric electronics'

For processor applications, the power dissipated in a nanostructure is a critical issue. Note that most effects of high-field interaction with dielectrics are reversible, so that the absorbed power is returned to the field at the end of the pulse. In conventional processors, most heat is produced when a transistor recharges the interconnect wire, resulting in a dissipation energy per switching of $Q_{switch} \approx 1/2 C_{interconnect}(\Delta U_{gate})^2 \approx 1$ fJ. In contrast, all-optical processors have no electrostatic charging of interconnect wires. In our case of a dielectric in a strong-pulse field, the heat released is equal to the excitation energy $\Delta_g \approx 10$ eV per real population of the electrons phototransferred from the valence band to the conduction band. This yields in a dissipation per switch of $Q_{switch} \approx \Delta_g \sigma A/e$, where σ is the transferred charge density and A is the cross-section of the excitation area. In experiments described in ref. 119, the phototransferred charge is $Q_p \approx 1$ fC per unit excitation cross-section (~3×10^{-5} cm^{-2}), which yields $\sigma \approx 3 \times 10^4$ fC cm^{-2}. Plasmonic concentration makes it possible to produce an optical switch with a size of ~10 nm, which is sufficiently small for large-scale integration. Assuming $A \approx 5$ nm^2, we obtain $Q_{switch} \approx 10$ aJ.

frequency with respect to bandgap, ω_L/Δ_g. This is expected to render processes more adiabatic (reversible). However, the interaction time should still remain shorter than the electron collision time ($\lesssim 50$ fs) to prevent dephasing[105,109]. Because the underlying processes are largely adiabatic, which causes the absorbed power to be returned to the field at the end of the switching laser pulse, heat dissipation per switching may be much lower than that of conventional semiconductor electronics (see Box 2 for an estimation and the average power requirements). Only further research will be able to determine whether dissipation due to real carriers can be sufficiently suppressed for dielectric-based logic to become a reality in the future. Our qualitative considerations seek to motivate further attosecond research in this fascinating direction.

Although the utility of the recently discovered reversible strong-field effects for signal processing will be verified only in the future, their applicability to advancing high-speed solid-state metrology to the petahertz frontier appears to be quite realistic on the basis of the first experiments. Indeed, by making some refinements, the current measured as a function of delay between the injection and drive laser fields in ref. 119 will directly indicate the temporal evolution of the field, the bandwidth of which was ~0.2 PHz in the original experiment. Hence, a solid-state petahertz-bandwidth oscilloscope capable of measuring light waveforms (recently demonstrated in the gas phase[121]) is within the realm of reality.

Attosecond physics: the next decade

Some 12 years after the first demonstration of a time-resolved measurement with a sub-femtosecond sampling signal[18] (in other words, attosecond metrology), the field of attosecond physics has come of age. Its key tools and techniques have been tried and tested, and are now being rapidly adopted all over the world. It is time to apply our recently gained ability to track and control electrons in atoms, molecules and solids to problems of direct relevance to life, technology and, potentially, medicine. In this Review, we have addressed how controlled light fields and attosecond measurement techniques may be instrumental in pushing the speed frontier of digital electronics. Direct time-domain insight into electronic motion will also be important for understanding the inner workings of the building blocks of life, namely biomolecules and their complexes. Such knowledge will have ramifications for biotechnologies as well as medical therapies, which involve very complicated electron processes in highly complex systems. The next decade will reveal whether attosecond science and technology is capable of rising to this challenge.

References

1. Krehl, P. & Engemann, S. August Toepler — the first who visualized shock waves. *Shock Waves* **5,** 1–18 (1995).
2. Abraham, H. & Lemoine, T. Disparition instantanée du phénomène de Kerr. *Compt. Rend. (Paris)* **129,** 206–208 (1899).
3. Schawlow, A. L. & Townes, C. H. Infrared and optical masers. *Phys. Rev.* **112,** 1940–1949 (1958).
4. Maiman, T. H. Stimulated optical radiation in ruby. *Nature* **187,** 493–494 (1960).
5. Franken, P. A., Hill, A. E., Peters, C. W. & Weinreich, G. Generation of optical harmonics. *Phys. Rev. Lett.* **7,** 118–119 (1961).
6. Armstrong, J. A., Bloembergen, N., Ducuing, J. & Pershan, P. S. Interactions between light waves in a nonlinear dielectric. *Phys. Rev.* **127,** 1918–1939 (1962).
7. Boyd, R. W. *Nonlinear optics* 2nd edn (Academic, 2003).
8. Diels, J.-C. & Rudolph, W. *Ultrashort Laser Pulse Phenomena: Fundamentals, Techniques, and Applications on a Femtosecond Time Scale* 2nd edn (Academic, 2006).
9. Fork, R. L., Brito Cruz, C. H., Becker, P. C. & Shank, C. V. Compression of optical pulses to six femtoseconds by using cubic phase compensation. *Opt. Lett.* **12,** 483–485 (1987).
10. Brabec, T. & Krausz, F. Intense few-cycle laser fields: frontiers of nonlinear optics. *Rev. Mod. Phys.* **72,** 545–591 (2000).
11. Szipöcs, R., Ferencz, K., Spielmann, C. & Krausz, F. Chirped multilayer coatings for broadband dispersion control in femtosecond lasers. *Opt. Lett.* **19,** 201–203 (1994).
12. Zewail, A. H. Femtochemistry: atomic-scale dynamics of the chemical bond. *J. Phys. Chem. A* **104,** 5660–5694 (2000).
13. Agostini, P., Fabre, F., Mainfray, G., Petite, G. & Rahman, N. K. Free-free transitions following six-photon ionization of xenon atoms. *Phys. Rev. Lett.* **42,** 1127–1130 (1979).
14. McPherson, A. *et al.* Studies of multiphoton production of vacuum-ultraviolet radiation in the rare gases. *J. Opt. Soc. Am. B* **4,** 595–601 (1987).
15. Ferray, M. *et al.* Multiple-harmonic conversion of 1064 nm radiation in rare gases. *J. Phys. B* **21,** L31–L35 (1988).
16. Macklin, J. J., Kmetec, J. D. & Gordon, C. L. III. High-order harmonic generation using intense femtosecond pulses. *Phys. Rev. Lett.* **70,** 766–769 (1993).
17. L'Huillier, A. & Balcou, P. High-order harmonic generation in rare gases with a 1-ps 1053-nm laser. *Phys. Rev. Lett.* **70,** 774–777 (1993).
18. Hentschel, M. *et al.* Attosecond metrology. *Nature* **414,** 509–513 (2001).
19. Agostini, P. & DiMauro, L. F. The physics of attosecond light pulses. *Rep. Prog. Phys.* **67,** 813–855 (2004).
20. Krausz, F. & Ivanov, M. Attosecond physics. *Rev. Mod. Phys.* **81,** 163–234 (2009).
21. Paulus, G. G. *et al.* Absolute-phase phenomena in photoionization with few-cycle laser pulses. *Nature* **414,** 182–184 (2001).
22. Xu, L. *et al.* Route to phase control of ultrashort light pulses. *Opt. Lett.* **21,** 2008–2010 (1996).
23. Telle, H. R. *et al.* Carrier-envelope offset phase control: a novel concept for absolute optical frequency measurement and ultrashort pulse generation. *Appl. Phys. B* **69,** 327–332 (1999).
24. Apolonski, A. *et al.* Controlling the phase evolution of few-cycle light pulses. *Phys. Rev. Lett.* **85,** 740–743 (2000).
25. Holzwarth, R. *et al.* Optical frequency synthesizer for precision spectroscopy. *Phys. Rev. Lett.* **85,** 2264–2267 (2000).
26. Jones, D. J. *et al.* Carrier-envelope phase control of femtosecond mode-locked lasers and direct optical frequency synthesis. *Science* **288,** 635–639 (2000).
27. Udem, T., Holzwarth, R. & Hänsch, T. W. Optical frequency metrology. *Nature* **416,** 233–237 (2002).
28. Baltuska, A. *et al.* Attosecond control of electronic processes by intense light fields. *Nature* **421,** 611–615 (2003).
29. Yakovlev, V. S. & Scrinzi, A. High harmonic imaging of few-cycle laser pulses. *Phys. Rev. Lett.* **91,** 153901 (2003).
30. Corkum, P. B. Plasma perspective on strong field multiphoton ionization. *Phys. Rev. Lett.* **71,** 1994–1997 (1993).
31. Kulander, K. C., Schafe, K. J. & Krause, J. L. in *Super-intense Laser-atom Physics* (eds Piraux, B., L'Huillier, A. & Rzazewski, K.) 507 (NATO ASI Series B, Plenum, 1993).
32. Schafer, K. J., Yang, B., DiMauro, L. F. & Kulander, K. C. Above threshold ionization beyond the high harmonic cutoff. *Phys. Rev. Lett.* **70,** 1599–1602 (1993).
33. Lewenstein, M., Balcou, P., Ivanov, M. Y., L'Huillier, A. & Corkum, P. B. Theory of high-harmonic generation by low-frequency laser fields. *Phys. Rev. A* **49,** 2117–2132 (1994).
34. Kienberger, R. *et al.* Atomic transient recorder. *Nature* **427,** 817–821 (2004).
35. Itatani, J. *et al.* Attosecond streak camera. *Phys. Rev. Lett.* **88,** 173903 (2002).
36. Kitzler, M., Milosevic, N., Scrinzi, A., Krausz, F. & Brabec, T. Quantum theory of attosecond XUV pulse measurement by laser dressed photoionization. *Phys. Rev. Lett.* **88,** 173904 (2002).
37. Mairesse, Y. & Quéré, F. Frequency-resolved optical gating for complete reconstruction of attosecond bursts. *Phys. Rev. A* **71,** 011401 (2005).
38. Quéré, F., Mairesse, Y. & Itatani, J. Temporal characterization of attosecond XUV fields. *J. Mod. Optics* **52,** 339–360 (2005).
39. Smirnova, O., Yakovlev, V. S. & Ivanov, M. Use of electron correlation to make attosecond measurements without attosecond pulses. *Phys. Rev. Lett.* **94,** 213001 (2005).
40. Yakovlev, V. S., Bammer, F. & Scrinzi, A. Attosecond streaking measurements. *J. Mod. Optics* **52,** 395–410 (2005).
41. Antoine, P., L'Huillier, A. & Lewenstein, M. Attosecond pulse trains using high-order harmonics. *Phys. Rev. Lett.* **77,** 1234–1237 (1996).
42. Paul, P. M. *et al.* Observation of a train of attosecond pulses from high harmonic generation. *Science* **292,** 1689–1692 (2001).
43. López-Martens, R. *et al.* Amplitude and phase control of attosecond light pulses. *Phys. Rev. Lett.* **94,** 033001 (2005).

44. Niikura, H. *et al.* Sub-laser-cycle electron pulses for probing molecular dynamics. *Nature* **417,** 917–922 (2002).
45. Johnsson, P. *et al.* Attosecond electron wave packet dynamics in strong laser fields. *Phys. Rev. Lett.* **95,** 013001 (2005).
46. Remetter, T. *et al.* Attosecond electron wave packet interferometry. *Nature Phys.* **2,** 323–326 (2006).
47. Mauritsson, J. *et al.* Attosecond pulse trains generated using two color laser fields. *Phys. Rev. Lett.* **97,** 013001 (2006).
48. Johnsson, P., Mauritsson, J., Remetter, T., L'Huillier, A. & Schafer, K. J. Attosecond control of ionization by wave-packet interference. *Phys. Rev. Lett.* **99,** 233001 (2007).
49. Mauritsson, J. *et al.* Coherent electron scattering captured by an attosecond quantum stroboscope. *Phys. Rev. Lett.* **100,** 073003 (2008).
50. Klünder, K. *et al.* Probing single-photon ionization on the attosecond time scale. *Phys. Rev. Lett.* **106,** 143002 (2011).
51. Niikura, H. *et al.* Probing molecular dynamics with attosecond resolution using correlated wave packet pairs. *Nature* **421,** 826–829 (2003).
52. Itatani, J. *et al.* Tomographic imaging of molecular orbitals. *Nature* **432,** 867–871 (2004).
53. Niikura, H., Villeneuve, D. M. & Corkum, P. B. Mapping attosecond electron wave packet motion. *Phys. Rev. Lett.* **94,** 083003 (2005).
54. Kanai, T., Minemoto, S. & Sakai, H. Quantum interference during high-order harmonic generation from aligned molecules. *Nature* **435,** 470–474 (2005).
55. Baker, S. *et al.* Probing proton dynamics in molecules on an attosecond time scale. *Science* **312,** 424–427 (2006).
56. Manfred, L. Molecular imaging using recolliding electrons. *J. Phys. B* **40,** R135–R173 (2007).
57. Smirnova, O. *et al.* High harmonic interferometry of multi-electron dynamics in molecules. *Nature* **460,** 972–977 (2009).
58. Wörner, H. J., Bertrand, J. B., Kartashov, D. V., Corkum, P. B. & Villeneuve, D. M. Following a chemical reaction using high-harmonic interferometry. *Nature* **466,** 604–607 (2010).
59. Shiner, A. D. *et al.* Probing collective multi-electron dynamics in xenon with high-harmonic spectroscopy. *Nature Phys.* **7,** 464–467 (2011).
60. Wörner, H. J. *et al.* Conical intersection dynamics in NO_2 probed by homodyne high-harmonic spectroscopy. *Science* **334,** 208–212 (2011).
61. Meckel, M. *et al.* Laser-induced electron tunneling and diffraction. *Science* **320,** 1478–1482 (2008).
62. Akagi, H. *et al.* Laser tunnel ionization from multiple orbitals in HCl. *Science* **325,** 1364–1367 (2009).
63. Blaga, C. I. *et al.* Imaging ultrafast molecular dynamics with laser-induced electron diffraction. *Nature* **483,** 194–197 (2012).
64. Huismans, Y. *et al.* Time-resolved holography with photoelectrons. *Science* **331,** 61–64 (2011).
65. Boguslavskiy, A. E. *et al.* The multielectron ionization dynamics underlying attosecond strong-field spectroscopies. *Science* **335,** 1336–1340 (2012).
66. Sansone, G. *et al.* Isolated single-cycle attosecond pulses. *Science* **314,** 443–446 (2006).
67. Goulielmakis, E. *et al.* Single-cycle nonlinear optics. *Science* **320,** 1614–1617 (2008).
68. Cavalieri, A. L. *et al.* Attosecond spectroscopy in condensed matter. *Nature* **449,** 1029–1032 (2007).
69. Schultze, M. *et al.* Delay in photoemission. *Science* **328,** 1658–1662 (2010).
70. Uiberacker, M. *et al.* Attosecond real-time observation of electron tunnelling in atoms. *Nature* **446,** 627–632 (2007).
71. Eckle, P. *et al.* Attosecond ionization and tunneling delay time measurements in helium. *Science* **322,** 1525–1529 (2008).
72. Mauritsson, J. *et al.* Attosecond electron spectroscopy using a novel interferometric pump-probe technique. *Phys. Rev. Lett.* **105,** 053001 (2010).
73. Kelkensberg, F. *et al.* Molecular dissociative ionization and wave-packet dynamics studied using two-color XUV and IR pump-probe spectroscopy. *Phys. Rev. Lett.* **103,** 123005 (2009).
74. Sansone, G. *et al.* Electron localization following attosecond molecular photoionization. *Nature* **465,** 763–766 (2010).
75. Goulielmakis, E. *et al.* Real-time observation of valence electron motion. *Nature* **466,** 739–744 (2010).
76. Wirth, A. *et al.* Synthesized light transients. *Science* **334,** 195–200 (2011).
77. Föhlisch, A. *et al.* Direct observation of electron dynamics in the attosecond domain. *Nature* **436,** 373–376 (2005).
78. Neppl, S. *et al.* Attosecond time-resolved photoemission from core and valence states of magnesium. *Phys. Rev. Lett.* **109,** 087401 (2012).
79. Zhang, C.-H. & Thumm, U. Attosecond photoelectron spectroscopy of metal surfaces. *Phys. Rev. Lett.* **102,** 123601 (2009).
80. Schiessl, K., Tökési, K., Solleder, B., Lemell, C. & Burgdörfer, J. Electron guiding through insulating nanocapillaries. *Phys. Rev. Lett.* **102,** 163201 (2009).
81. Lemell, C., Solleder, B., Tökési, K. & Burgdörfer, J. Simulation of attosecond streaking of electrons emitted from a tungsten surface. *Phys. Rev. A* **79,** 062901 (2009).
82. Kazansky, A. K. & Echenique, P. M. One-electron model for the electronic response of metal surfaces to subfemtosecond photoexcitation. *Phys. Rev. Lett.* **102,** 177401 (2009).
83. Krasovskii, E. E., Silkin, V. M., Nazarov, V. U., Echenique, P. M. & Chulkov, E. V. Dielectric screening and band-structure effects in low-energy photoemission. *Phys. Rev. B* **82,** 125102 (2010).
84. Krasovskii, E. E. Attosecond spectroscopy of solids: streaking phase shift due to lattice scattering. *Phys. Rev. B* **84,** 195106 (2011).
85. Zhang, C.-H & Thumm, U. Streaking and Wigner time delays in photoemission from atoms and surfaces. *Phys. Rev. A* **84,** 033401 (2011).
86. Zhang, C.-H. & Thumm, U. Effect of wave-function localization on the time delay in photoemission from surfaces. *Phys. Rev. A* **84,** 065403 (2011).
87. Keldysh, L. V. Behavior of non-metallic crystals in strong electric fields. *Sov. Phys. JETP* **33,** 763–770 (1957).
88. Stockman, M. I. & Hewageegana, P. Absolute phase effect in ultrafast optical responses of metal nanostructures. *Appl. Phys. A* **89,** 247–250 (2007).
89. Krüger, M., Schenk, M. & Hommelhoff, P. Attosecond control of electrons emitted from a nanoscale metal tip. *Nature* **475,** 78–81 (2011).
90. Piglosiewicz, B. *et al.* Carrier-envelope phase effects on the strong-field photoemission of electrons from metallic nanostructures. *Nature Photon.* **8,** 37–42 (2014).
91. Herink, G., Solli, D. R., Gulde, M. & Ropers, C. Field-driven photoemission from nanostructures quenches the quiver motion. *Nature* **483,** 190–193 (2012).
92. Stockman, M. I., Kling, M. F., Kleineberg, U. & Krausz, F. Attosecond nanoplasmonic field microscope. *Nature Photon.* **1,** 539–544 (2007).
93. Kahng, D. Electric field controlled semiconductor device. US patent 3,102,230 (1963).
94. Taur, Y. & Ning, T. H. *Fundamentals of Modern VLSI Devices* (Cambridge Univ. Press, 1998).
95. Liou, J. J. & Schwierz, F. *Modern Microwave Transistors: Theory, Design and Performance* (Wiley, 2003).
96. Schwierz, F., Wong, H. & Liou, J. J. *Nanometer CMOS* (Pan Stanford, 2010).
97. Rodwell, M. J. W. *et al.* Submicron scaling of HBTs. *IEEE T. Electron. Dev.* **48,** 2606–2624 (2001).
98. Miyamoto, Y. *et al.* InP hot electron transistors with a buried metal gate. *Jpn. J. Appl. Phys. 1* **42,** 7221–7226 (2003).
99. Burke, P. J. AC performance of nanoelectronics: towards a ballistic THz nanotube transistor. *Solid-State Electron.* **48,** 1981–1986 (2004).
100. Jimenez, D., Iniguez, B., Sune, J. & Saenz, J. J. Analog performance of the nanoscale double-gate metal-oxide-semiconductor field-effect-transistor near the ultimate scaling limits. *J. Appl. Phys.* **96,** 5271–5276 (2004).
101. Ortolani, M. *et al.* Imaging the coupling of terahertz radiation to a high electron mobility transistor in the near-field. *J. Eur. Opt. Soc. Rapid Pub.* **4,** 09006 (2009).
102. El Fatimy, A. *et al.* Plasma wave field effect transistor as a resonant detector for 1 terahertz imaging applications. *Opt. Commun.* **282,** 3055–3058 (2009).
103. Kim, D. H. & del Alamo, J. A. 30-nm InAs PHEMTs with f_T = 644 GHz and f_{max} = 681 GHz. *IEEE Electron. Device Lett.* **31,** 806–808 (2010).
104. Papaioannou, S. *et al.* A 320 Gb/s-throughput capable 2 × 2 silicon-plasmonic router architecture for optical interconnects. *J. Lightwave Technol.* **29,** 3185–3195 (2011).
105. Stockman, M. I. Nanoplasmonics: past, present, and glimpse into future. *Opt. Express* **19,** 22029–22106 (2011).
106. Han, Z. & Bozhevolnyi, S. I. Radiation guiding with surface plasmon polaritons. *Rep. Prog. Phys.* **76,** 016402 (2013).
107. Bozhevolnyi, S. I., Volkov, V. S., Devaux, E., Laluet, J. Y. & Ebbesen, T. W. Channel plasmon subwavelength waveguide components including interferometers and ring resonators. *Nature* **440,** 508–511 (2006).
108. Ghimire, S. *et al.* Observation of high-order harmonic generation in a bulk crystal. *Nature Phys.* **7,** 138–141 (2011).
109. Gertsvolf, M., Spanner, M., Rayner, D. M. & Corkum, P. B. Demonstration of attosecond ionization dynamics inside transparent solids. *J. Phys. B* **43,** 131002 (2010).
110. Schultze, M. *et al.* Controlling dielectrics with the electric field of light. *Nature* **493,** 75–78 (2013).
111. Mitrofanov, A. V. *et al.* Optical detection of attosecond ionization induced by a few-cycle laser field in a transparent dielectric material. *Phys. Rev. Lett.* **106,** 147401 (2011).
112. Bardeen, J. & Brattain, W. H. The transistor, a semi-conductor triode. *Phys. Rev.* **74,** 230–231 (1948).
113. Wannier, G. H. *Elements of Solid State Theory* (Cambridge Univ. Press, 1959).

114. Schiffrin, A. *et al.* Addendum to "Optical-field-induced current in dielectrics." *Nature* http://dx.doi.org/10.1038/nature13077 (in the press).

115. Yamanishi, M. Field-induced optical nonlinearity due to virtual transitions in semiconductor quantum well structures. *Phys. Rev. Lett.* **59,** 1014–1017 (1987).

116. Chemla, D. S., Miller, D. A. B. & Schmitt-Rink, S. Generation of ultrashort electrical pulses through screening by virtual populations in biased quantum wells. *Phys. Rev. Lett.* **59,** 1018–1021 (1987).

117. Yablonovitch, E., Heritage, J. P., Aspnes, D. E. & Yafet, Y. Virtual photoconductivity. *Phys. Rev. Lett.* **63,** 976–979 (1989).

118. Hu, B. B., Zhang, X.-C. & Auston, D. H. Terahertz radiation induced by subband-gap femtosecond optical excitation of GaAs. *Phys. Rev. Lett.* **67,** 2709–2712 (1991).

119. Schiffrin, A. *et al.* Optical-field-induced current in dielectrics. *Nature* **493,** 70–74 (2013).

120. Khurgin, J. Optically induced currents in dielectrics as a nonlinear optical effect. Preprint at http://arXiv.org/abs/1303.3994 (2013).

121. Kim, K. T. *et al.* Petahertz optical oscilloscope. *Nature Photon.* **7,** 958–962 (2013).

122. Landau, L. D. & Lifshitz, E. M. *Electrodynamics of Continuous Media: Volume 8* 2nd edn (Pergamon, 1984).

123. Packan, P. *et al.* High performance 32nm logic technology featuring 2nd generation high-k + metal gate transistors in *2009 IEEE International Electron Devices Meeting (IEDM)* 1–4 (2009).

124. Pasricha, S. & Dutt, N. *On-chip Communication Architectures: System on Chip Interconnect* (Morgan Kaufmann, 2008).

125. Corkum, P. & Krausz, F. Attosecond science. *Nature Phys.* **3,** 381–387 (2007).

126. Bohr, M. & Mistry, K. *Intel's revolutionary 22 nm transistor technology* http://download.intel.com/newsroom/kits/22nm/pdfs/22nm-Details_Presentation.pdf (2011).

Additional information

Reprints and permissions information is available online at www.nature.com/reprints. Correspondence and requests for materials should be addressed to F.K. and M.I.S.

Competing financial interests

The authors declare no competing financial interests.